Insoluble surfactant spreading along thin liquid films confined by chemical surface patters

PCCP

Cite this: *Phys. Chem. Chem. Phys.*, 2011, **13**, 9768–9777

www.rsc.org/pccp

PAPER

Insoluble surfactant spreading along thin liquid films confined by chemical surface patterns

David K. N. Sinz, Myroslava Hanyak, Jos C. H. Zeegers and Anton A. Darhuber*

Received 12th October 2010, Accepted 18th March 2011
DOI: 10.1039/c0cp02135k

We conducted a combined experimental and numerical study of the spreading of insoluble surfactants on spatially confined thin liquid films. We found that the spreading dynamics can locally be represented by a power-law relation $x \sim t^{\alpha}$. We determine the time evolution of the liquid film thickness and the corresponding spreading exponents α both from experiments using interference microscopy and numerical finite element simulations. The lateral confinement induces non-uniform height- and surface velocity profiles, which manifest themselves in a pronounced transition of the evolving rivulet morphology. Excellent agreement between experimental and simulation results has been achieved.

I. Introduction

The spreading dynamics of liquids is of crucial importance for numerous technological applications ranging from printing and coating processes,[1] pulmonary drug delivery[2] to crude oil recovery.[3] In the context of oil recovery, up to about 60% of the originally present crude oil remains in a reservoir after the so-called primary and secondary recovery phases.[3] Injection of surfactant solutions is considered a potential means for extracting a larger fraction of the oil[4,5] owing to two different mechanisms. Surfactant-induced reductions of interfacial tension facilitate deformations of oil–brine interfaces and therefore oil extraction. Furthermore, non-uniform surfactant distributions at fluid–fluid interfaces give rise to interfacial tension gradients and associated Marangoni stresses, which locally cause flow from regions of lower to regions of higher interfacial tension.[6–8] The first mechanism acts primarily in rock pores that are accessible to pressure-driven flow from injection- to production wells. In addition, the second one can be utilized to transport surfactant and wettability modifiers along dead-end pores that are inaccessible to pressure-driven transport, provided a largely continuous liquid–liquid interface exists.

Oil and surfactant spreading along the surface of deep liquid layers has been investigated by Fay[9] and Hoult.[10] Huh *et al.*[11] studied the spreading rate of a thin liquid on an immiscible liquid substrate by means of experiments and an approximate quasi-steady analysis. The driving force was assumed to be a combination of gravity and interfacial forces. Foda and Cox[12] considered the spreading of a thin liquid film on a water–air interface for the case where surface tension gradients drive the motion. Camp and Berg[13] performed experiments regarding the unidirectional spreading of several pure oils and oil–surfactant mixtures on water in the surface-tension regime and reported data consistent with the similarity solution of Foda and Cox.[12] The leading edge position L of a spreading oleic acid film was determined to scale with time as $L \sim t^{\alpha}$ with the spreading exponent $\alpha = 3/4$. Dagan[14] considered surfactant spreading in the regime where inertial effects cannot be ignored and recovered the $L \sim t^{3/4}$ relation with a prefactor proportional to $-\Gamma_s \partial\gamma/\partial\Gamma$, where γ is the surface tension, Γ is the surfactant surface concentration and Γ_s is the constant source concentration. Jensen[15] presented a detailed theoretical study and showed that for spreading over uncontaminated layers $L \approx ((\partial\gamma/\partial\Gamma)^2 t^3)^{1/[2(n+2)]}$ where $n = 1$ for a strip geometry and $n = 2$ for a droplet. For pre-contaminated layers he derived the asymptotic scaling $L \sim t^{3/4}$ for both strip- and droplet geometries. Joos and van Hunsel[16] considered the spreading of droplets of surfactant solutions on immiscible organic liquids and found a spreading exponent of 3/4 for a solution of a fluorinated surfactant on CCl_4. For a different material combination Svitova *et al.*[17] reported spreading dynamics that cannot be represented by a power law and that proceeded slower for pure dodecane than for a substantially more viscous mineral oil as the sub-phase. Berg[18] performed surfactant spreading experiments along a flat interface between deep, immiscible fluid layers and observed the spreading exponent $\alpha = 3/4$.

Surfactant spreading at the air–liquid interface of thin liquid films has been studied extensively in the past.[2,19–35] Ahmad and Hansen[19] reported on the spreading of oleic acid on glycerol films and found a spreading exponent of $\alpha = 0.5$. Using experiments and theoretical models based on the lubrication approximation, Troian *et al.*[21] as well as Grotberg

Mesoscopic Transport Phenomena Group, Department of Applied Physics, Eindhoven University of Technology, Postbus 513, 5600MB Eindhoven, The Netherlands. E-mail: A.A.Darhuber@tue.nl

and co-workers[20,22,24] investigated axisymmetric unsteady spreading of surfactant monolayers on thin liquid films. Film thinning occurred in the vicinity of the deposited surfactant as well as film thickening and the formation of a rim occurred near the surfactant leading edge. Jensen and Grotberg presented a model for the spreading of soluble surfactants[25] considering linearized sorption kinetics and fast vertical diffusion across the film thickness. Different solubilities of the surfactant induced qualitative differences in the flow patterns. Jensen[26] discussed similarity solutions of surfactant driven flow problems. Starov *et al.* treated the spreading of a drop of a surfactant solution over a thin water film as a two-stage process.[27] In a first stage the surface concentration was kept constant to account for micellar dissolution, followed by a second stage where after micelle depletion the total mass of the surfactant adsorbed at the surface was assumed constant.

Troian *et al.*,[21] Frank and Garoff,[36] He and Ketterson,[37] Matar and Troian,[28,29] Cachile *et al.*,[38,39] Fischer and Troian,[32,33] Afsar-Siddiqui *et al.*,[40–42] Warner *et al.*[34] and Jensen and Naire[35] considered instabilities occurring near the perimeter of spreading surfactant droplets and surfactant fronts. Evans *et al.* investigated the role of surfactants in the formation of crater defects in drying paint layers.[31] Dussaud *et al.* studied the dynamics of insoluble surfactant monolayers spreading on glycerol films.[43] Experimental film thickness profiles were obtained by means of Moire topography. A spreading exponent of $\alpha = 0.23$ was found, which is close to the analytically predicted value for radial spreading of a finite quantity of the deposited surfactant. Craster and Matar[44] elucidated the effect of autophobing of surfactant solutions. The combined effect of temperature and surfactant concentration gradients was studied by Borhan *et al.*, Chen and Stebe, Chen *et al.*, Edmonstone and Matar, as well as Hanumanthu and Stebe.[45–49]

In the context of pulmonary surfactant transport, several groups investigated exogenous surfactant spreading along thin liquid films adhering to the interior surface of hollow tubes.[50–53] Davis *et al.*[50] studied axisymmetric and steady flows and reported that in the limit of negligible radial interface curvature, *i.e.* when the tube radius R is very much larger than the adhering film thickness h, *i.e.*, $\delta \equiv h/R \rightarrow 0$, the flow is solely influenced by surface tension gradients. A qualitatively different behavior was predicted for small but finite δ. Espinosa *et al.*[51] found that the effect of circumferential curvature was negligible, as if spreading occurred over a flat surface. For a linear equation of state a spreading exponent $\alpha = \frac{1}{3}$ was reported. Furthermore, the presence of a resident endogenous surfactant amplified the spreading rate. Williams and Jensen[52] considered the effect of circumferential non-uniformities of the liquid film thickness and concluded that flow-induced shape deformations of the liquid lining influence the spreading dynamics only weakly. Follows *et al.*[54] applied neutron scattering and observed the presence of multilayers at the surface of exogenous lung surfactant solutions. The authors recommended that their presence be incorporated into the existing models, which are largely based on the assumption that surfactants adsorb as monolayers.

In order to facilitate a quantitative comparison between experiments and numerical simulations in the context of surfactant-assisted enhanced oil recovery, we study the spreading of insoluble surfactants along thin liquid films deposited on chemically patterned surfaces. Hydrophilic and hydrophobic patterns confine the location and flow of liquid to predefined regions on the substrate in the shape of long and narrow stripes. The translational invariance of the stripe geometry enables comparison with earlier results for one-dimensional spreading along films of constant thickness. We investigate the consequences of geometrical confinement and the non-zero curvature of the interface on the surfactant spreading dynamics as a first step towards more complex, branched and three-dimensional geometries encountered in porous media.

In Section II we describe the sample fabrication, the experimental setup and procedure. Typical experimental results are presented in Section III. In Section IV we outline the theoretical model for the spreading dynamics of insoluble surfactants on thin liquid films along with its numerical implementation. Numerical results are presented in Section V, followed by a detailed comparison with extensive experimental data in Section VI.

II. Experimental procedure

Chemically patterned surfaces were fabricated using self-assembled monolayers of 1*H*,1*H*,2*H*,2*H*-perfluorooctyl-trichlorosilane (PFOTS, purity >97%, Sigma Aldrich product number 448931) on single-side polished Si substrates with dimensions of typically 50 mm × 50 mm × 0.7 mm. The substrates were cut from Silicon wafers (n-type doped with Ph) with a diameter of 150 mm obtained from Silicon Quest (batch number SQ13869). They were cleaned in two steps: first by immersion in a solution of hydrogen peroxide (30%, J.T. Baker product number 7047) and sulfuric acid (95%, J.T. Baker product number 6057), mixed at a volume ratio of 1 : 1, and subsequently by exposure to an oxygen plasma. The chemical surface patterns were created by photolithography and subsequent vapor deposition of PFOTS in a sealed glass jar at a temperature of 100 °C, *i.e.* the hydrophilic regions were masked with photo-resist and the hydrophobic ones were left unmasked prior to the vapor deposition. The hydrophilic patterns used in the experiments described here were of rectangular shape with a width of $w < 1.5$ mm and a length of $L = 40$–70 mm. The aforedescribed patterning procedure resulted in an advancing contact angle for glycerol between 70° and 90° on the hydrophobic areas with sufficient spatial uniformity and fidelity of the patterned structure, which is essential for the reproducibility of the measurements.

Before deposition of the sub-phase liquid in the individual experiments, the hydrophilic regions were repeatedly cleaned using the aforementioned mixture of hydrogen peroxide and sulfuric acid. Liquid films (rivulets) of anhydrous glycerol (purity 99%, Sigma Aldrich product number 49767, density $\rho = 1.26$ g cm^{-3}, surface tension $\gamma = 63.4$ mN m^{-1})[55] with a center thickness in the range of $h_0 = 1$–10 μm were deposited on the hydrophilic regions of the substrates using spin-coating, ensuring uniform and reproducible height profiles. A typical interference microscopy image of a rivulet prior to surfactant deposition is shown in Fig. 1(a). Films with a thickness above $h_0 = 80$ μm were deposited using a micro-syringe since

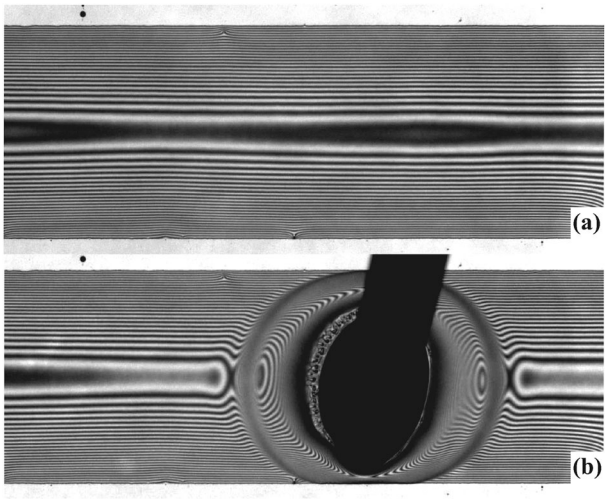

Fig. 1 Interference microscopy images of a rivulet height profile (a) prior to and (b) during deposition of a droplet of oleic acid. Rivulet width $w = 1.5$ mm and initial center height $h_0 = 6.6$ μm.

capillary equilibrium is then reached in an acceptably short time. We determined the viscosity at the temperature at which our experiments were conducted as $\mu(25\ ^\circ\mathrm{C}) = (876 \pm 3)$ mPa s using a Brookfield DV-II + Pro viscosimeter which agrees with literature values[56,57] for pure, anhydrous glycerol.

After deposition of the sub-phase, typically 0.1 to 0.2 μl of the insoluble surfactant *cis*-9-octadecenoic acid (oleic acid, purity 99%, Sigma Aldrich product number O1008, density $\rho_{\mathrm{oleic}} = 0.895$ g cm^{-3}, surface tension[58] $\gamma_{\mathrm{oleic}}(25\ ^\circ\mathrm{C}) = 32.5$ mN m^{-1}, viscosity[59] $\mu_{\mathrm{oleic}}(25\ ^\circ\mathrm{C}) = 28.2$ mPa s) were deposited in the center of the rivulets using a micro-syringe as a dip-pen [Fig. 1(b)]. Oleic acid is a surface-active substance that is practically insoluble in glycerol.[24] The dependence of the glycerol surface tension γ on the oleic acid surface concentration Γ has been measured by Gaver and Grotberg.[24] As shown in Fig. 2 we fitted their experimental data with the following expression:

$$\gamma = \gamma_{\mathrm{m}} + \Pi_{\mathrm{max}} \exp(-\bar{A}\Gamma^2/\Gamma_0^2), \qquad (1)$$

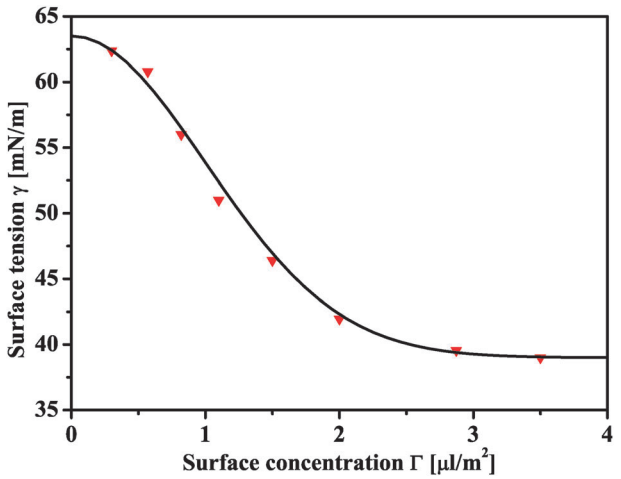

Fig. 2 Dependence of the glycerol surface tension γ on the oleic acid surface concentration Γ. Experimental data[24] are indicated by triangles. The continuous line is a fit according to $\gamma = \gamma_{\mathrm{m}} + \Pi_{\mathrm{max}} \exp(-\bar{A}\Gamma^2/\Gamma_0^2)$ with a fit parameter $\bar{A} = 6.125$.

where $\Pi_{\mathrm{max}} = 24$ mN m^{-1} is the maximum spreading pressure, $\gamma_{\mathrm{m}} = 39$ mN m^{-1} is the asymptotic value of the surface tension, $\Gamma_0 \equiv 3.5$ μl m^{-2} and $\bar{A} = 6.125$ is a fit parameter. Thus, we consider a realistic, non-linear equation of state $\gamma(\Gamma)$ connecting surface tension and surface concentration for this material system.

The dynamics after surfactant deposition were monitored by means of interference microscopy using an Olympus BX51 upright microscope. Depending on the sub-phase film height, the illuminating light was passband-limited around a center wavelength of $\lambda = 750$ nm or $\lambda = 550$ nm with a bandpass of $\Delta\lambda = 10$ nm providing a height resolution of 10–20 nm. In the case of film heights above $h_0 = 80$ μm the evolution of the rivulet height profile was observed in a side-view configuration using a telecentric lens with a vertical resolution of approximately 5–10 μm. All experiments have been performed in a horizontal sample orientation with the liquid deposited on the upper side of the substrates.

III. Exemplary experimental results

Fig. 3(a) shows a series of exemplary interference microscopy images obtained for a rivulet of width $w = 0.28$ mm. The deposition of the surfactant locally reduces the sub-phase surface tension and induces Marangoni stresses that in the case of thin liquid films cause a net flow away from the deposition region. A local maximum in the height profile is visible in Fig. 3(a), which is propagating along the rivulets as marked by the red arrows. The very early stage of the rim propagation is shown in Fig. 1(b), where two half-moon shaped ridges are visible left and right of the deposited surfactant droplet. Their positions are a measure of the advance of the surfactant monolayer along the rivulet.[24] In the immediate vicinity of the deposited surfactant droplet, a pronounced film thinning is observed in Fig. 3(a). Concluding from the grayscale values of the interference microscopy images, the local film thickness is well below 100 nm. We introduce a Cartesian coordinate system with the x-axis parallel to the rivulet and the z-axis normal to the substrate surface, *i.e.* opposite to the direction of gravity. The position $x = 0$ corresponds to the right edge of the surfactant droplet; $y = 0$ corresponds to the centerline of the rivulet, see Fig. 3(a).

In Fig. 3(b) exemplary centerline height profiles $h(x, y = 0, t)$ are presented for different times after deposition. These profiles were obtained from an analysis of the corresponding interference fringe patterns. The peak height of the rim h_{max} was determined to be approximately $1.6h_0$ at $t = 6$ s. In later stages of the experiment the width of the rim grows and we observe an increase in the peak height to about $2h_0$. Fig. 3(c) shows typical measurements of the rim position as a function of time $x_{\mathrm{rim}}(t)$ for various values of h_0. The rim propagates faster along thicker rivulets. To very good approximation the experimental data can be represented by a power law relation $x_{\mathrm{rim}} \sim t^{\alpha}$. The solid lines in Fig. 3(c) correspond to power law fits with exponents α in the range of 0.32–0.34 apparently independent of h_0. The spreading exponent α quantifies the displacement efficiency of a given surfactant in a certain geometry of the chemical surface patterning.

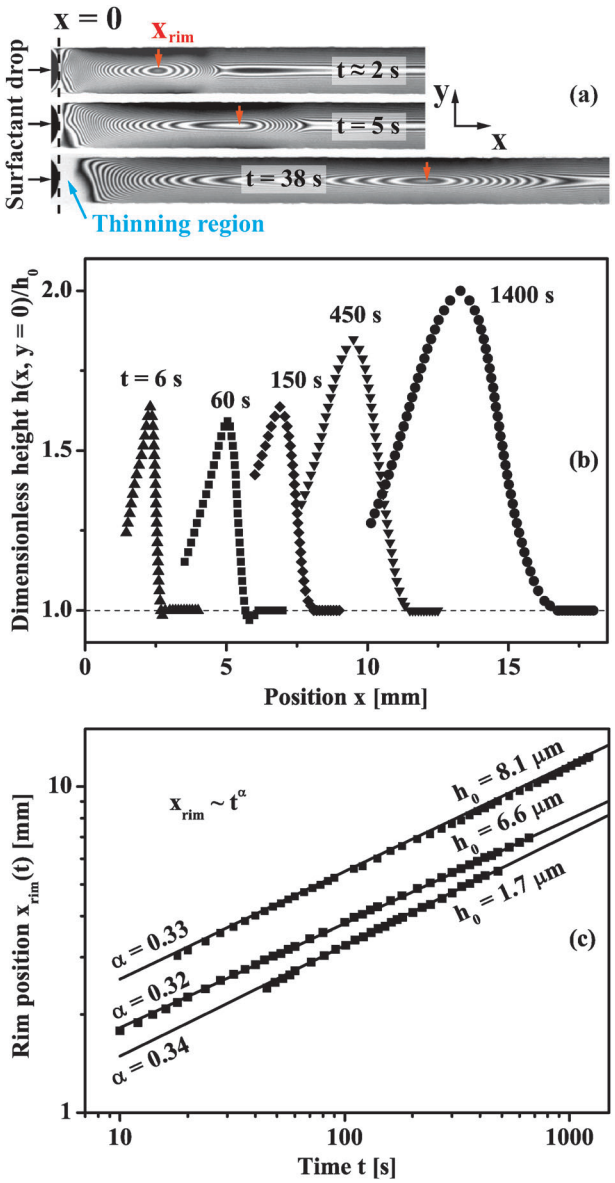

Fig. 3 (a) Interference microscopy images of rivulet height profiles at different times t = 2 s, 5 s and 38 s after surfactant deposition. The black circle segment visible at the left margin of the images is part of the deposited surfactant droplet. The red arrows indicate the rim position. The blue arrow marks the region of strong film thinning adjacent to the surfactant droplet. Rivulet width w = 0.28 mm. (b) Experimentally measured rivulet height profiles $h(x, y = 0, t)$ at different times after the deposition of a surfactant droplet. Rivulet width w = 1.5 mm. (c) Exemplary measurements of the rim position as a function of time for various initial film heights and a rivulet width of w = 1.5 mm.

IV. Mathematical model for insoluble surfactant spreading

We consider the spreading of an insoluble surfactant on a thin liquid film of constant Newtonian viscosity. Chemical patterning confines the liquid to a stripe of width w and length L as shown in Fig. 4. Since the lateral aspect ratio $\varepsilon \equiv 2h_0/w \ll 1$, the small-slope approximation can be applied to derive an

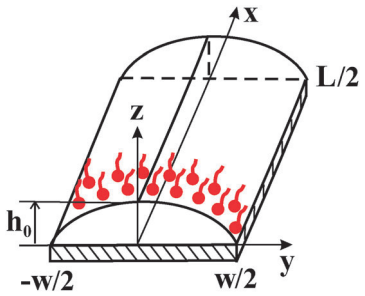

Fig. 4 Sketch of the initial condition of the rivulet geometry with initial surfactant distribution.

evolution equation for the sub-phase height profile[60] that accounts for the influence of Marangoni stresses, hydrostatic and capillary pressure gradients. Borgas and Grotberg[20] and Troian *et al.*[23] derived an equation for surfactant surface transport including the effects of convection by the liquid surface motion as well as surface diffusion.

Using the non-dimensional variables

$$\bar{x} = \frac{2x}{w}, \quad \bar{y} = \frac{2y}{w}, \quad \bar{h} = \frac{h}{h_0} \tag{2}$$

$$\bar{\Gamma} = \frac{\Gamma}{\Gamma_0}, \quad \bar{p} = \frac{pw^2}{4h_0\Pi_{\max}}, \quad \bar{t} = t\frac{4h_0\Pi_{\max}}{\mu w^2}, \tag{3}$$

we arrive at the following non-dimensional system of equations

$$\frac{\partial \bar{h}}{\partial \bar{t}} + \bar{\nabla}\left[\frac{1}{2}(\bar{h}^2\bar{\nabla}\bar{\gamma}) - \frac{\mathrm{Bo}}{3}\bar{h}^3\bar{\nabla}\bar{h} - \frac{\varepsilon^2}{3}\bar{h}^3\bar{\nabla}\bar{p}\right] = 0 \tag{4}$$

$$\frac{\partial \bar{\Gamma}}{\partial \bar{t}} + \bar{\nabla}\left[\bar{h}\bar{\Gamma}\bar{\nabla}\bar{\gamma} - \frac{\mathrm{Bo}}{2}\bar{h}^2\bar{\Gamma}\bar{\nabla}\bar{h} - \frac{\varepsilon^2}{2}\bar{h}^2\bar{\Gamma}\bar{\nabla}\bar{p} - \frac{1}{\mathrm{Pe_s}}\bar{\nabla}\bar{\Gamma}\right] = 0 \tag{5}$$

$$\bar{p} = -\bar{\gamma}\bar{\nabla}^2\bar{h} \tag{6}$$

$$\bar{\gamma} = \frac{\gamma_m}{\Pi_{\max}} + \exp(-\bar{A}\bar{\Gamma}^2), \tag{7}$$

where $\mathrm{Bo} \equiv \rho g h_0^2/\Pi_{\max}$ is the Bond number, $\mathrm{Pe_s} \equiv h_0\Pi_{\max}/(\mu D_s)$ is the surface Peclet number, μ and ρ are the fluid viscosity and density, respectively, and D_s represents the surfactant surface diffusivity. The second term in eqn (4) and (5) represents the influence of Marangoni stresses arising from gradients in surface tension $\bar{\gamma}$. The third term in both equations accounts for hydrostatic pressure gradients and the fourth term reflects capillary pressure gradients. The last term in eqn (5) describes surface diffusion along the liquid–air interface. Eqn (6) corresponds to the Laplace–Young equation. Eqn (7) is the non-dimensional version of eqn (1).

The system of eqn (4)–(7) is solved numerically with the finite element software Comsol Multiphysics 3.5 using the following boundary conditions (BCs)

$$\frac{\partial \bar{h}}{\partial \bar{x}}(0,\bar{y},\bar{t}) = 0 = \frac{\partial \bar{h}}{\partial \bar{y}}(\bar{x},0,\bar{t}) \tag{8}$$

$$\frac{\partial \bar{\Gamma}}{\partial \bar{x}}(0,\bar{y},\bar{t}) = 0 = \frac{\partial \bar{\Gamma}}{\partial \bar{y}}(\bar{x},0,\bar{t}) \tag{9}$$

$$\frac{\partial \bar{p}}{\partial \bar{x}}(0,\bar{y},\bar{t}) = 0 = \frac{\partial \bar{p}}{\partial \bar{y}}(\bar{x},0,\bar{t}) \tag{10}$$

$$\bar{h}(\bar{x},\,1,\,\bar{t}) = 0 \tag{11}$$

$$\frac{\partial \bar{\Gamma}}{\partial \bar{y}}(\bar{x},1,\bar{t}) = 0 \tag{12}$$

$$\bar{h}(\infty,\,\bar{y},\,\bar{t}) = \bar{f}(\bar{y}) \tag{13}$$

$$\bar{\Gamma}(\infty,\,\bar{y},\,\bar{t}) = 0 \tag{14}$$

$$\frac{\partial \bar{p}}{\partial \bar{x}}(\infty,\bar{y},\bar{t}) = 0, \tag{15}$$

where $\bar{f}(\bar{y})$ is the boundary height profile corresponding to the static equilibrium. If the influence of gravity is negligible, the static equilibrium profile is parabolic $\bar{f}(\bar{y}) = 1 - \bar{y}^2$.

Eqn (8)–(10) reflect the mirror symmetry of the system with respect to the planes $\bar{x} = 0$ and $\bar{y} = 0$. Boundary conditions (11 and 12) correspond to a vanishing film thickness and surfactant flux at the edge of the hydrophilic stripe. Eqn (13) and (14) represent a clean, surfactant-free liquid surface at a large distance away from the surfactant deposition region. Eqn (15) expresses that liquid cannot leave the computational domain as a consequence of pressure gradients, which is physically not entirely realistic. However, since the initial height profile is independent of $\bar{x}$ and since the domain length $L/2$ is always chosen larger than the leading edge position of the spreading surfactant front, this BC has no influence on the system dynamics.

The following initial conditions (ICs) are used for the height profile and pressure

$$\bar{h}(\bar{x},\bar{y},0) = \bar{f}(\bar{y}),\quad \bar{p}(\bar{x},\bar{y},0) = -\bar{\gamma}\frac{\partial^2 \bar{f}}{\partial \bar{y}^2}. \tag{16}$$

We consider two cases regarding the IC for the surfactant distribution:

(1) In the case of *finite surfactant supply*, a limited initial quantity of the surfactant is distributed uniformly in the stripe $0 \le \bar{x} \le \bar{x}_0$

$$\bar{\Gamma}(\bar{x},\,0) = \tfrac{1}{2}(1 - \tanh[B(\bar{x} - \bar{x}_0)]), \tag{17}$$

which subsequently depletes during the spreading process. Here, $B \equiv 10$ defines the steepness of the initial concentration distribution. The parameter $\bar{x}_0$ quantifies the longitudinal dimension of the area that is (initially) covered with the surfactant.

(2) In our experiments, however, the deposited surfactant quantity is large and does not deplete as fast as in the finite supply model. To mimic such a *continuous surfactant supply*, we impose a constant surface concentration in the region of surfactant deposition, *i.e.*, $\bar{\Gamma}(0 \le \bar{x} \le \bar{x}_0, \bar{y}, \bar{t}) = \text{const}$, and we maintain continuity of the state variables at $\bar{x} = \bar{x}_0$.

V. Numerical results

A Finite surfactant supply

Fig. 5 shows typical snapshots of the surfactant spreading process represented by the film thickness isolines for dimensionless times $\bar{t}$ from 0 to 1000. As in experiments, we observe film thinning in the vicinity of the deposition region and development of a rim, which is advancing along the rivulet. The rim widens in time and propagates in the x-direction with the maximum located at the rivulet centerline $\bar{y} = 0$. Fig. 6(a) and (b) show the time evolution of the height profile $\bar{h}(\bar{x},\ \bar{y} = 0,\ \bar{t})$ and the surfactant concentration $\bar{\Gamma}(\bar{x},\ \bar{y} = 0,\ \bar{t})$ at the rivulet centerline, with parameters $\varepsilon = 10^{-2}$, $\mathrm{Pe_s} = 10^3$, $\bar{x}_0 = 0.5$ and $\mathrm{Bo} = 0$. The surfactant depletes in time at the deposition region and redistributes along the rivulet surface. The time evolution of the rim position $\bar{x}_{\mathrm{rim}}$ is presented in Fig. 6(c). To good approximation the rim position $\bar{x}_{\mathrm{rim}}(t)$ follows a power law behavior $\bar{x}_{\mathrm{rim}} \sim \bar{t}^{\alpha}$. The spreading exponents extracted from the data presented in Fig. 6(c) fall in the range 0.24–0.25, and are essentially independent of the aspect ratio ε. Nevertheless, these values are significantly smaller than the experimental results, for which the assumption of finite surfactant supply is not an accurate representation.

Fig. 7 compares the time evolution of the rim height $\bar{h}_{\max}$ for spreading along a rivulet (solid lines) with rectilinear, one-dimensional spreading along a thin liquid film of *uniform* thickness h_0 (dashed lines), *i.e.* in the limit of infinitely wide rivulets, $w \to \infty$. The rapid increase of $\bar{h}_{\max}(\bar{t} \lesssim 0.2)$ represents the rim formation in the early stage of the spreading process. For lower aspect ratios two local maxima in $\bar{h}_{\max}(\bar{t})$ are observed, whereas for $\varepsilon = 0.1$ only a single peak is present. Except in the vicinity of the second maximum in $\bar{h}_{\max}(\bar{t})$, the rim height is larger for one-dimensional spreading due to the absence of transverse curvature. Smaller aspect ratios tend to give larger dimensionless rim heights, since smaller capillary

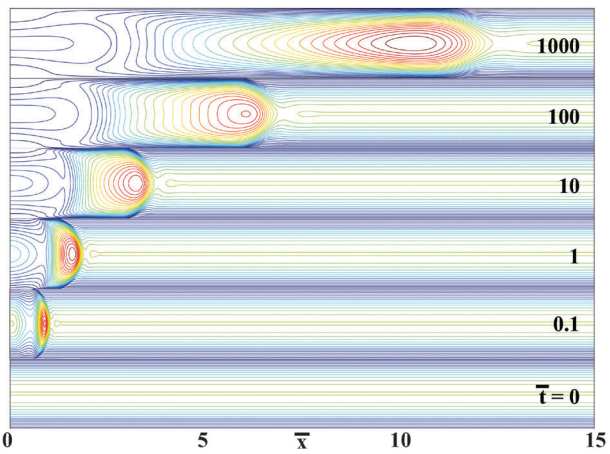

Fig. 5 Contours of rivulet height for finite surfactant supply at $\bar{t} = 0$, 0.1, 1, 10, 100, 1000 with $\bar{x}_0 = 0.5$, $\mathrm{Pe_s} = 50\,000$, $\varepsilon = 0.01$, and $\mathrm{Bo} = 0$.

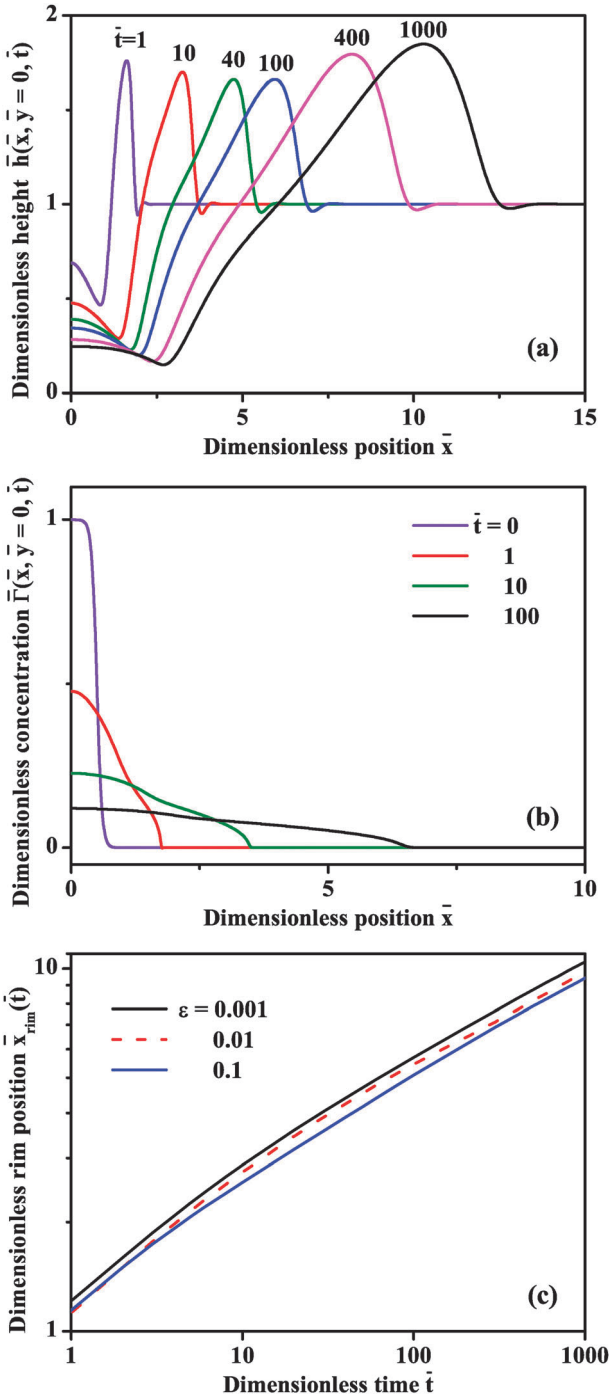

Fig. 6 (a) Evolution of the centerline height profile $\bar{h}(\bar{x}, \bar{y} = 0, \bar{t})$ for finite surfactant supply. (b) Dimensionless surfactant concentration $\bar{\Gamma}(\bar{x}, \bar{y} = 0, \bar{t})$. (c) Rim position $\bar{x}_{rim}(\bar{t})$. All data results have been obtained for parameter values $\bar{x}_0 = 0.5$, $Pe_s = 1000$, $\varepsilon = 0.01$, and $Bo = 0$.

pressure provides less of an opposing force to the height increase. Jensen[26] showed that for $\varepsilon \to 0$ and $Pe_s \to \infty$ the non-dimensional rim height equals 2 in the case of one-dimensional, rectilinear spreading.

During experiments surface active contaminants, either airborne or from within the sub-phase liquid, can adsorb on the liquid–air interface. We account for such a contamination

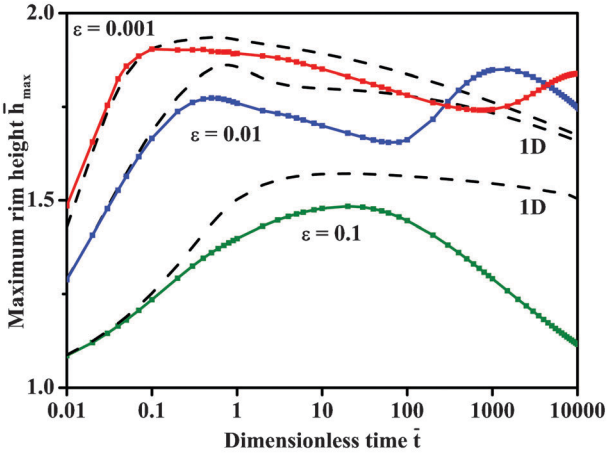

Fig. 7 Maximum height *vs.* dimensionless time for rivulets with finite surfactant supply (solid lines) compared to one-dimensional rectilinear spreading (dashed lines) for parameter values $\bar{x}_0 = 0.5$, $Pe_s = 1000$, and $Bo = 0$.

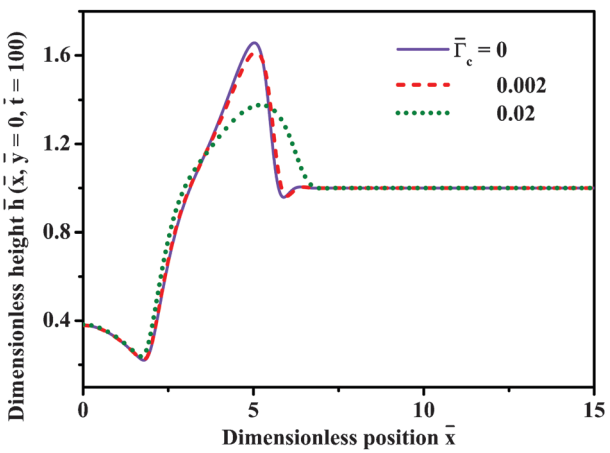

Fig. 8 Rivulet height profile for different pre-contaminated rivulets for parameter values $\bar{x}_0 = 0.5$, $Pe_s = 1000$, $\varepsilon = 0.01$, and $Bo = 0$.

by adding a constant term $\bar{\Gamma}_c$ to the initial concentration distribution in eqn (17)

$$\bar{\Gamma}(\bar{x}, 0) = \bar{\Gamma}_c + 0.5(1 - \tanh[B(\bar{x} - \bar{x}_0)]). \qquad (18)$$

The rim propagation dynamics along a pre-contaminated rivulet for a value of $\bar{\Gamma}_c = 0.02$ is essentially unaffected as compared to the case of $\bar{\Gamma}_c = 0$. However, already a contamination as small as 2%, which would be hard to detect experimentally, significantly reduces the rim height, as shown in Fig. 8, consistent with the findings of Dussaud *et al.*[43]

Not unexpectedly, a variation of the Peclet number Pe_s from 1000 to 50 000 shows negligible effect on the rim position for $\bar{t} < 1000$. Smaller Peclet numbers reduce the rim height $\bar{h}_{max}(\bar{t})$ consistent with the results of Gaver and Grotberg[22] for one-dimensional surfactant spreading on thin liquid films.

B Continuous surfactant supply

Fig. 9(a) and (b) depict the time evolution of the height profile and surfactant concentration in the case of continuous

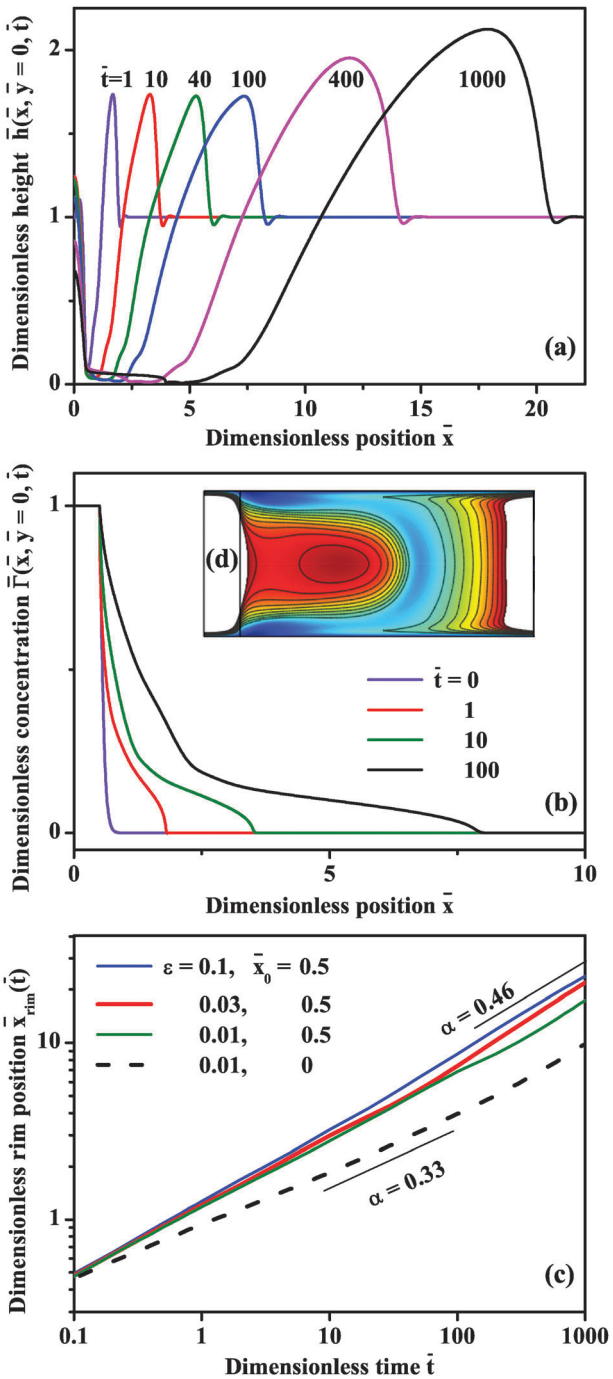

Fig. 9 (a) Evolution of the centerline height profile $\bar{h}(\bar{x}, \bar{y} = 0, \bar{t})$ for continuous surfactant supply, $\varepsilon = 0.01$ and $\bar{x}_0 = 0.5$. (b) Dimensionless surfactant concentration $\bar{\Gamma}(\bar{x}, \bar{y} = 0, \bar{t})$ for $\varepsilon = 0.01$ and $\bar{x}_0 = 0.5$. (c) Rim position $\bar{x}_{rim}(\bar{t})$ for $\bar{x}_0 = 0.5$ (solid lines) and $\bar{x}_0 = 0$ (dashed line). All data results have been obtained for parameter values $Pe_s = 1000$, and $Bo = 0$. (d) Sub-phase expulsion at $\bar{t} = 200$ for continuous surfactant supply and $\varepsilon = 0.03$.

surfactant supply. The film thinning in the vicinity of the surfactant deposition area is significantly stronger than in the case of finite supply, because the constant surfactant concentration in the area $\bar{x} < \bar{x}_0$ sustains large surface tension gradients.

In Fig. 9(c) we present the rim position for different aspect ratios. The corresponding spreading exponents $\alpha = 0.40$–0.46, fitted in the interval $10 < \bar{t} < 1000$, are higher compared to the case of finite surfactant supply, and an increased influence of the aspect ratio on the rim position $\bar{x}_{rim}$ is apparent. The curves corresponding to aspect ratios $\varepsilon = 0.03$ and 0.01 exhibit an increase in the spreading exponent approximately at times $\bar{t} = 50$ and 200. These transitions are preceded by a process of sub-phase expulsion,[61] *i.e.* the ejection of liquid that was previously located in the area of surfactant deposition, as illustrated in Fig. 9(d) at $\bar{t} = 200$ for $\varepsilon = 0.03$. The dashed line in Fig. 9(c) corresponds to the rim position for an infinitely narrow surfactant deposition area, $\bar{x}_0 = 0$. No expulsion is observed in this case, which causes a slight reduction of the spreading exponent $\alpha(\bar{t} = 1000)$ by 0.02 as compared to the case of $\bar{x}_0 = 0.5$.

VI. Discussion

The early stages of the spreading dynamics are strongly influenced by the experimental deposition process as well as the ICs and BCs of the numerical model. For a quantitative comparison of experimental and numerical results, we therefore focus on later stages of the spreading process. While the principal setups of our experiments and numerical simulations are similar, there are slight differences in the deposition process. In the numerical simulations, surfactants are introduced as a dense monolayer on top of the initially *undisturbed* rivulet profile. Depending on the type of simulation, the amount of the surfactant in the deposition area is then depleted or held constant during the course of the simulation. In our experiments, however, a large amount of the surfactant is deposited onto the rivulet. Furthermore, due to the manual deposition technique the droplet is not placed instantaneously and flushed on top of the undisturbed rivulet profile but part of the underlying liquid is squeezed out during deposition. The relatively large amount of the surfactant in the droplet ensures a continuous supply during the course of an experiment. Consequently, the numerical studies of surfactant spreading with a continuous supply can be expected to resemble the experimental conditions after initial effects have decayed.

In Fig. 10(a) we present fitted power law exponents α for a large range of aspect ratios $\varepsilon = 2h_0/w$. Experimental exponents were obtained for rivulet widths of $w = 1.5$ mm and $w = 0.28$ mm as indicated in Fig. 10 by solid symbols. The smaller rivulet width w allowed the application of interference microscopy for higher aspect ratios since this method is limited to film thicknesses below approximately 10 μm. Exponents extracted from the numerical simulations for continuous supply and $\bar{x}_0 = 0.5$ in Fig. 9(c) are represented by red up-triangles. Blue down-triangles designate numerical results for $\bar{x}_0 = 0$, where no sub-phase expulsion occurred, resulting in slightly reduced spreading exponents α that agree with the experimental data very well. The exponents corresponding to the blue down-triangles in Fig. 10(a) were fitted to the simulation results in the time interval $10 \leq \bar{t} \leq 100$, which is comparable to the experimental range.

At the edges of the surfactant source area, *i.e.* around $\bar{x} = \bar{x}_0$, the subphase film thickness rapidly thins as depicted

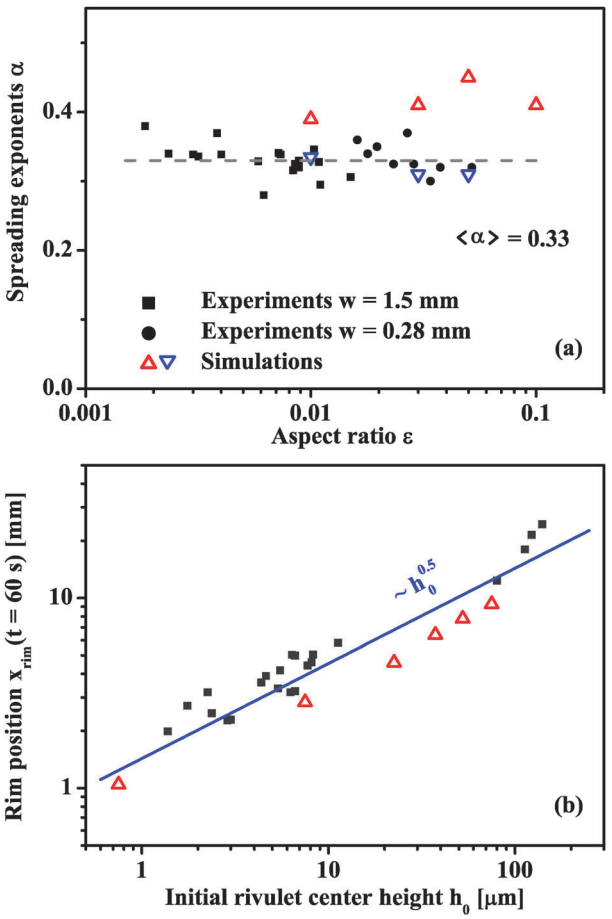

Fig. 10 (a) Spreading exponents α as a function of the aspect ratio ε. Black symbols indicate experimental results measured on rivulets of width $w = 1.5$ mm (squares) and $w = 0.28$ mm (circles). The average experimental value of $\langle\alpha\rangle = 0.33$ is indicated by the gray dashed line. Simulation results for $\bar{x}_0 = 0.5$ (red up-triangles) exhibited sub-phase expulsion while this was not observed for $\bar{x}_0 = 0$ (blue down-triangles). (b) Rim position 60 s after surfactant deposition as a function of the initial film height for $w = 1.5$ mm. Experimental data and numerical results for $\bar{x}_0 = 0.5$ are given by black squares and red triangles, respectively. The scaling behavior $x_{\mathrm{rim}}(t = 60\ \mathrm{s}) \approx \sqrt{h_0}$ is indicated by the solid blue line.

in Fig. 9(a). This implies that—except for the case of $\bar{x}_0 = 0$—a volume of the subphase liquid becomes temporarily immobilized underneath the surfactant and is gradually discharged at a later time [Fig. 9(d)]. This delayed subphase release has a noticeable effect on the spreading exponent as shown in Fig. 10(a).

Fig. 10(b) shows the rim position 60 s after deposition, $x_{\mathrm{rim}}(60\ \mathrm{s})$, as a function of the initial rivulet center height h_0 for $w = 1.5$ mm. Filled symbols represent experimental data, and open triangles indicate numerical simulations. Assuming that the rim propagation rate $\frac{\mathrm{d}x_{\mathrm{rim}}}{\mathrm{dt}}$ scales with the Marangoni velocity $h_0\tau/\mu$ and that the streamwise surface tension gradient $\tau = \partial\gamma/\partial x$ scales as $\tau \sim \Pi_{\max}/x_{\mathrm{rim}}$, where $\Pi_{\max}$ is the spreading pressure, we expect

$$\frac{\mathrm{d}x_{\mathrm{rim}}}{\mathrm{dt}} \approx \frac{h_0\Pi_{\max}}{\mu x_{\mathrm{rim}}} \rightarrow x_{\mathrm{rim}} \approx \sqrt{2\frac{h_0\Pi_{\max}}{\mu}}\,t, \qquad (19)$$

and thus a power law relation $x_{\mathrm{rim}} \sim \sqrt{h_0}$. The solid line in Fig. 10(b) corresponds to a power law relation $x_{\mathrm{rim}}(t = 60\ \mathrm{s}) \sim \sqrt{h_0}$ and is an excellent approximation to both experimental and numerical results.

The numerically obtained peak positions in Fig. 10 appear to systematically lie slightly below the experimental values. A probable reason for this offset is water absorption from the ambient atmosphere due to the hygroscopic nature of glycerol. Already a water weight fraction as low as 3% results in a viscosity decrease of roughly 50% in the relevant temperature range.[56] The plotted simulation results were converted to dimensional values assuming the viscosity of pure glycerol at 25 °C.

In both experiments and simulations we observe a systematic change in the peak height and shape of the rim as it propagates along the rivulet. Initially the rim exhibits a considerable asymmetry in the streamwise direction, which gradually disappears at later stages. The asymmetry at early stages manifests itself in the longitudinal spacing of the interference fringes, which is more dense ahead of the peak position than behind it, as depicted in Fig. 11(a). In Fig. 11(b) this asymmetry, which is especially pronounced for low aspect ratio experiments, has largely disappeared.

In Fig. 12 we plot the non-dimensional rim height $h_{\max}/h_0$ as a function of time for different values of ε. During the initial

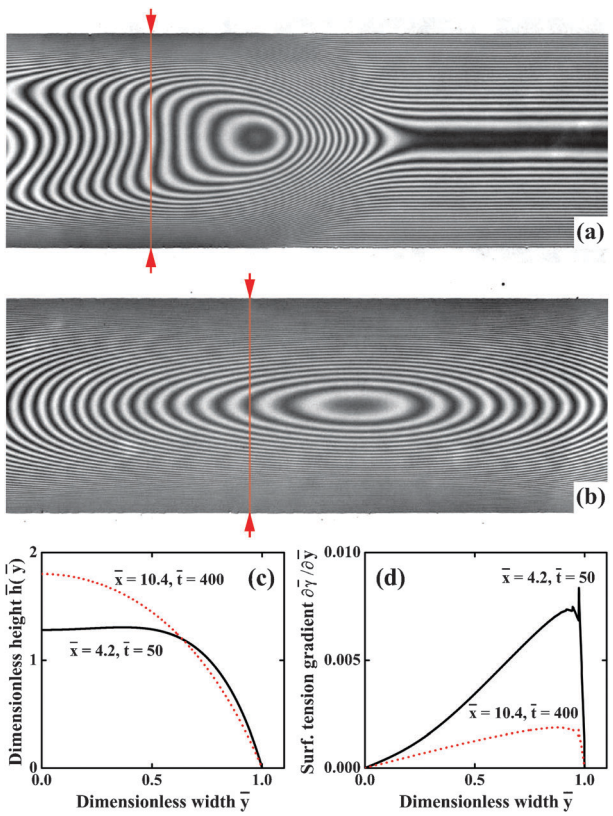

Fig. 11 Interference microscopy images of the propagating rim at (a) an early stage ($t = 30$ s) and (b) a later stage ($t = 250$ s). (c) Transverse height profile $\bar{h}(\bar{y}, \bar{t})$ for times $\bar{t} = 50$ and $\bar{t} = 400$ located at the distance $w/2$, behind the rim. (d) Surface tension gradient in the y-direction $\partial\bar{\gamma}/\partial\bar{y}$ for $\bar{t} = 50$ and $\bar{t} = 400$ located at the distance of $w/2$, behind the rim. Input parameters for (c) and (d) are $\bar{x}_0 = 0.5$, $\mathrm{Pe}_s = 1000$, $\varepsilon = 0.01$, and $\mathrm{Bo} = 0$.

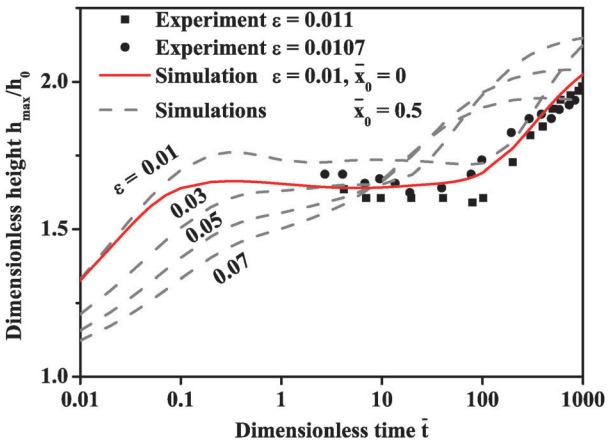

Fig. 12 Dimensionless rim height $\bar{h}_{max}(\bar{t})$ for different values of ε. The dashed lines correspond to numerical simulations for continuous supply of the surfactant over a deposition region of length $\bar{x}_0 = 0.5$. The solid line represents a simulation for $\bar{x}_0 = 0$. Symbols represent experimental data obtained for $w = 1.5$ mm and aspect ratios of $\varepsilon = 0.011$ (squares) and $\varepsilon = 0.0107$ (circles).

formation process of the rim, a rapid increase of h_{max} for times below $\bar{t} = 0.2$ is observed in the numerical simulations. For an aspect ratio $\varepsilon = 0.01$ the rim height then effectively reaches a plateau value. At later times a pronounced increase of h_{max} occurs for all investigated aspect ratios. The experimental data obtained for $\varepsilon \approx 0.01$ (represented by circles and squares in Fig. 12) reproduce this behavior very well, both with respect to the onset time and amplitude of the peak height increase. The gray dashed lines in Fig. 12 correspond to simulations with a deposition region of length $\bar{x}_0 = 0.5$, which leads to a sub-phase expulsion process and thus to slightly higher values of the rim height h_{max}. Numerical results for the case of $\bar{x}_0 = 0$ are represented by the solid line. The latter do not exhibit any sub-phase expulsion and are in almost perfect quantitative agreement with the experimental data.

We attribute the increase in the rim height to changes in the transverse rivulet height profile, which are a consequence of declining lateral surface tension gradients. The transverse height profile at the position of the red markers in Fig. 11 exhibits a strong flattening in the middle of the rivulet as evidenced by the straight trajectory of the interference fringes. At a later time [Fig. 11(b)] this flattening has disappeared and the rivulet cross-section is to good approximation parabolic. The same behavior is observed in the numerical simulations depicted in Fig. 11(c), where the dimensionless height profile $\bar{h}(\bar{x}_{rim} - 1, \bar{y})$ at a distance of half a rivulet width behind the peak position is plotted for two different times.

This qualitative difference in the height profiles is caused by lateral concentration gradients originating from the non-uniform surface velocity profile. As the driving force of the spreading process is Marangoni stress, the flow velocity scales with the local film thickness. Since the film thickness is 0 at the boundaries of the hydrophilic stripe, the streamwise velocity is higher in the middle of the rivulet as compared to its edges. The lateral shear in the velocity distribution initially leads to a non-uniform surfactant surface distribution $\Gamma(y)$. Darhuber *et al.*[62] studied rivulet shape distortions as a consequence of transverse temperature gradients and identified the relevant non-dimensional number as $\tau/(\varepsilon p_{cap})$ where p_{cap} is the capillary pressure. As soon as the value of $\tau = \nabla_{\|}\gamma$ falls below a certain threshold, the shape distortion vanishes and the parabolic cross-section is restored. We conjecture that the same mechanism is the origin of the shape distortions in Fig. 11(a–d). This is supported by Fig. 11(d) where a strong decay of the lateral surface tension gradient at positions and times corresponding to the curves in Fig. 11(c) is evident. The relaxation of the transverse height profile towards a parabolic shape implicates an increase in the center height, which explains the increase in rim height h_{max} observed in Fig. 12. Larger values of the aspect ratio ε are associated with a higher lateral curvature and hence an increased capillary pressure, which acts as the restoring force for the transition in the height profile. Consequently the transition occurs earlier for larger aspect ratios. We note that an increase in the peak height observed for one-dimensional spreading can only occur due to sub-phase expulsion[61] and that the effect observed in Fig. 12 is a consequence of lateral confinement due to chemical patterning.

VII. Summary and conclusion

We conducted an experimental and numerical study of surfactant spreading on narrow glycerol rivulets defined by chemical surface patterning of flat impenetrable substrates. Using interference microscopy and a numerical model based on the lubrication approximation, we monitored the evolution of the liquid height profile after deposition of an insoluble surfactant droplet at the rivulet–air interface. The spreading dynamics can locally be well approximated by a power-law $x \sim t^{\alpha}$. We found that for uniform initial rivulet height profiles, the initial film thickness has little effect on the spreading exponents. Continuous, *i.e.* unlimited surfactant supply led to higher exponents and increased the influence of the rivulet aspect ratio as compared to the case of limited supply. The spreading exponents determined from quasi-continuous-supply experiments ($\alpha = 0.33 \pm 0.04$) compare favorably with those numerically obtained. The lateral confinement induces non-uniform height- and surface velocity profiles, which manifest themselves in a pronounced transition of the evolving rivulet morphology.

Acknowledgements

The authors would like to thank Steffen Berg and Axel Makurat from Shell International Exploration and Production (Rijswijk, The Netherlands) for the inspiring collaboration. The authors gratefully acknowledge that this research is supported partially by the Dutch Technology Foundation STW, applied science division of NWO and the Technology Program of the Ministry of Economic Affairs.

References

1 P. M. Schweizer and S. F. Kistler, *Liquid Film Coating*, Chapman & Hall, London, 1997.
2 J. B. Grotberg, *Annu. Rev. Fluid Mech.*, 1994, **26**, 529–571.
3 L. W. Lake, *Enhanced oil recovery*, Prentice-Hall, New Jersey, 1989.
4 D. O. Shan and R. S. Schechter, *Improved oil recovery by surfactant and polymer flooding*, Academic Press Inc., New York, 1977.

5 L. L. Schramm, *Surfactants: fundamentals and applications in the petroleum industry*, Cambridge University Press, Cambridge, 2000.
6 V. G. Levich, *Physicochemical Hydrodynamics*, Prentice-Hall, Englewood Cliffs, 1962.
7 C. S. Yih, *Phys. Fluids*, 1968, **11**, 477–480.
8 J. Adler and L. Sowerby, *J. Fluid Mech.*, 1970, **42**, 549–560.
9 *Oil on the Sea*, ed. J. A. Fay and D. P. Hoult, Plenum, N.Y., 1969, pp. 55–63.
10 D. P. Hoult, *Annu. Rev. Fluid Mech.*, 1972, **4**, 341–368.
11 C. Huh, M. Inoue and S. Mason, *Can. J. Chem. Eng.*, 1975, **53**, 367–371.
12 M. Foda and R. G. Cox, *J. Fluid Mech.*, 1980, **101**, 33–51.
13 D. W. Camp and J. C. Berg, *J. Fluid Mech.*, 1987, **184**, 445–462.
14 Z. Dagan, *PCH PhysicoChem. Hydrodyn.*, 1984, **5**, 43–51.
15 O. E. Jensen, *J. Fluid Mech.*, 1995, **293**, 349–378.
16 P. Joos and J. V. Hunsel, *J. Colloid Interface Sci.*, 1985, **106**, 161–167.
17 T. F. Svitova, R. M. Hill and C. J. Radke, *Langmuir*, 1999, **15**, 7392–7402.
18 S. Berg, *Phys. Fluids*, 2009, **21**, 032105.
19 J. Ahmad and R. S. Hansen, *J. Colloid Interface Sci.*, 1972, **38**, 601–604.
20 M. S. Borgas and J. B. Grotberg, *J. Fluid Mech.*, 1988, **193**, 151–170.
21 S. M. Troian, X. L. Wu and S. A. Safran, *Phys. Rev. Lett.*, 1989, **62**, 1496–1499.
22 D. P. Gaver and J. B. Grotberg, *J. Fluid Mech.*, 1990, **213**, 127–148.
23 S. M. Troian, E. Herbolzheimer and S. A. Safran, *Phys. Rev. Lett.*, 1990, **65**, 333–336.
24 D. P. Gaver and J. B. Grotberg, *J. Fluid Mech.*, 1992, **235**, 399–414.
25 O. E. Jensen and J. B. Grotberg, *Phys. Fluids A*, 1993, **5**, 58–68.
26 O. E. Jensen, *Phys. Fluids*, 1994, **6**, 1084–1094.
27 V. M. Starov, A. de Ryck and M. G. Velarde, *J. Colloid Interface Sci.*, 1997, **190**, 104–113.
28 O. K. Matar and S. M. Troian, *Phys. Fluids*, 1998, **10**, 1234–1236.
29 O. K. Matar and S. M. Troian, *Phys. Fluids*, 1999, **11**, 3232–3246.
30 J. L. Bull, L. K. Nelson, J. T. Walsh, Jr., M. R. Glücksberg, S. Schürch and J. B. Grotberg, *J. Biomed. Eng.*, 1999, **121**, 89–98.
31 P. L. Evans, L. W. Schwartz and R. V. Roy, *J. Colloid Interface Sci.*, 2000, **227**, 191–205.
32 B. J. Fischer and S. M. Troian, *Phys. Fluids*, 2003, **15**, 3837.
33 B. J. Fischer and S. M. Troian, *Phys. Rev. E: Stat. Phys., Plasmas, Fluids, Relat. Interdiscip. Top.*, 2003, **67**, 016309.
34 M. R. E. Warner, R. V. Craster and O. K. Matar, *J. Fluid Mech.*, 2004, **510**, 169–200.
35 O. E. Jensen and S. Naire, *J. Fluid Mech.*, 2006, **554**, 5–24.
36 B. Frank and S. Garoff, *Langmuir*, 1995, **11**, 87–93.
37 S. He and J. B. Ketterson, *Phys. Fluids*, 1995, **7**, 2640–2647.
38 M. Cachile and A. M. Cazabat, *Langmuir*, 1999, **15**, 1515–1521.
39 M. Cachile, M. Schneemilch, A. Hamraoui and A. M. Cazabat, *Adv. Colloid Interface Sci.*, 2002, **96**, 59–74.
40 A. B. Afsar-Siddiqui, P. F. Luckham and O. K. Matar, *Langmuir*, 2003, **19**, 696–702.
41 A. B. Afsar-Siddiqui, P. F. Luckham and O. K. Matar, *Langmuir*, 2003, **19**, 703–708.
42 A. B. Afsar-Siddiqui, P. F. Luckham and O. K. Matar, *Adv. Colloid Interface Sci.*, 2003, **106**, 183–236.
43 A. D. Dussaud, O. K. Matar and S. M. Troian, *J. Fluid Mech.*, 2005, **544**, 23–51.
44 R. V. Craster and O. K. Matar, *Langmuir*, 2007, **23**, 2588–2601.
45 A. Borhan, H. Haj-Hariri and A. Nadim, *J. Colloid Interface Sci.*, 1992, **149**, 553–560.
46 J. Chen and K. J. Stebe, *J. Fluid Mech.*, 1997, **340**, 35–59.
47 Y. S. Chen, Y. L. Lu, Y. M. Yang and J. R. Maa, *Int. J. Multiphase Flow*, 1997, **23**, 325–335.
48 B. D. Edmonstone and O. K. Matar, *J. Colloid Interface Sci.*, 2004, **274**, 183–199.
49 R. Hanumanthu and K. J. Stebe, *Phys. Fluids*, 2007, **19**, 042103.
50 S. H. Davis, A. Liu and G. R. Sealy, *J. Fluid Mech.*, 1974, **62**, 737–751.
51 F. F. Espinosa, A. H. Shapiro, J. J. Fredberg and R. D. Kamm, *J. Appl. Physiol.*, 1993, **75**, 2028–2039.
52 H. A. R. Williams and O. E. Jensen, *J. Biomech. Eng.*, 2000, **122**, 159–166.
53 W. T. Tsai and L. Y. Liu, *Colloids Surf., A*, 2004, **234**, 51–62.
54 D. Follows, F. Tiberg, R. K. Thomas and M. Larsson, *Biochim. Biophys. Acta*, 2007, **1768**, 228–235.
55 A. A. Newman and L. V. Cocks, *Glycerol*, CRC Press, Cleveland, 1968.
56 J. B. Segur and H. E. Oberstar, *Ind. Eng. Chem.*, 1951, **43**, 2117–2120.
57 *CRC Handbook of Chemistry and Physics*, ed. D. Lide, CRC Press, Cleveland, 1982.
58 L. D. A. Chumpitaz, L. F. Coutinho and J. A. Meirelles, *J. Am. Oil Chem. Soc.*, 1999, **76**, 379–382.
59 H. Noureddini, B. C. Teoh and D. L. Clements, *J. Am. Oil Chem. Soc.*, 1992, **69**, 1189–1191.
60 A. Oron, S. H. Davis and S. G. Bankoff, *Rev. Mod. Phys.*, 1997, **69**, 931–980.
61 D. K. N. Sinz, M. Hanyak and A. A. Darhuber, to be published.
62 A. A. Darhuber, J. Z. Chen, J. M. Davis and S. M. Troian, *Philos. Trans. R. Soc London*, 2004, **362**, 1037–1058.